



# Facile construction of MoO<sub>3</sub>@ZIF-8 core-shell nanorods for efficient photoreduction of aqueous Cr (VI)

Yifan Zhang, Soo-Jin Park\*

Department of Chemistry and Chemical Engineering, Inha University, 100 Inharo, Incheon 22212, South Korea

## ARTICLE INFO

### Keywords:

MoO<sub>3</sub>@ZIF-8 core-shell nanorods  
Cr (VI) reduction  
Visible light  
Photocatalytic activity

## ABSTRACT

Recently, hexavalent chromium (Cr(VI)) in wastewater has become a threat to the ecosystem and human health. The synthesis of high-performance and recyclable photocatalysts still remains a challenge. The photoreduction efficiency of Cr(VI) is inhibited by the high rate of recombination of electron-hole pairs and the low adsorption capacity of Cr(VI). In this study, three-dimensional (3D) MoO<sub>3</sub>/ZIF-8 core-shell nanorod composite photocatalysts were prepared via a facile two-step method and applied to the reduction of Cr(VI). The chemical state of the elements, microstructure, surface elements, and optical properties of the MoO<sub>3</sub>/ZIF-8 core-shell nanorods were characterized by X-ray diffraction (XRD), Fourier transform infrared (FT-IR), scanning electron microscopy (SEM), transmission electron microscopy (TEM), X-ray photoelectron spectroscopy (XPS), and UV–vis diffuse reflectance spectroscopy. The as-prepared MoO<sub>3</sub>@ZIF-8 catalysts displayed superior photocatalytic activity for Cr(VI) reduction under visible light, compared to the pure ZIF-8 and MoO<sub>3</sub> nanowires. Further, MoO<sub>3</sub>@ZIF-8 (with 15% of ZIF-8) exhibited the best photocatalytic activity, and promoted 100% reduction of Cr(VI) (15 mg L<sup>-1</sup>) within 45 min. The 3-D core-shell structure not only provided a large surface area, but also separated the electron-hole pairs effectively. The photocatalytic activity of the composite remained almost unchanged after four cycles. The mechanism of Cr(VI) reduction is also discussed in detail.

## 1. Introduction

Recently, rapid industrialization has posed a serious threat to the environment, resulting in wastewater containing heavy ions becoming a primary concern for human beings. Chromium, as a typical heavy metal contaminant, is generated by commercial operations such as the leather tanning, textile manufacturing, and steel fabrication industries [1–5]. In contrast with other heavy metals, chromium exists in two main oxidation states: Cr(VI) and Cr(III). Cr(VI) has been regarded as a carcinogen due to its acute toxicity to organisms, whereas Cr(III) is nontoxic and acts as an essential trace metal for human beings [6–8]. Therefore, the reduction of Cr(VI) to Cr(III) is deemed to be an effective method for water treatment. Various pioneering works have been performed to resolve the issue of chromium reduction, and the approaches can be classified into three types: microbial reduction, chemical reduction, and photocatalytic reduction [9–12]. The photocatalytic reduction method is cost effective without the discharge of any perilous chemicals [13–18].

Metal-organic frameworks (MOFs), as a new class of organic-inorganic hybrid materials with high surface area and large pore volume, have attracted much attention in various applications such as gas

capture and storage, catalysis, drug delivery, and trace metal ion sensing [19–25]. Ongoing efforts are still being devoted to the modification of MOFs as photocatalysts. Most MOFs, such as ZIF-8 (bandgap: 5.1 eV), can only adsorb UV light due to the large bandgap, which limits the scope of application. To solve this problem, many strategies such as metal loading, dye sensing, organic linker decoration, and semiconductor combination have been developed to reduce the bandgap to expand the visible light utilization [26–31]. The combination of MOFs with semiconductors is regarded as an efficient way to improve the photocatalytic performance. With this in mind, various semiconductors have been used to construct coherent interfacial connections between MOFs and semiconductors in order to retard the recombination of photo-induced electron-hole pairs, thereby enhancing the photocatalytic activity. In 2014, Wu and co-workers developed a ternary UiO-66/CdS/RGO photocatalyst with a photocatalytic hydrogen evolution rate 13.8 times higher than that of commercial CdS [32]. The reduced electron-hole recombination rate and close contact of the catalyst components were the crucial factors giving rise to the enhanced photocatalytic activity. The modification of MOFs for the photoreduction of Cr(VI) is currently at the forefront of research. Various MOFs have been explored for Cr(VI) removal, including ZIF-8, UiO-66, and MIL-53.

\* Corresponding author.

E-mail address: [sjpark@inha.ac.kr](mailto:sjpark@inha.ac.kr) (S.-J. Park).

<https://doi.org/10.1016/j.apcatb.2018.08.077>

Received 29 June 2018; Received in revised form 24 August 2018; Accepted 29 August 2018

Available online 31 August 2018

0926-3373/ © 2018 Elsevier B.V. All rights reserved.

MOFs have also been loaded with noble metals such as Au, Pd, and Pt, leading to efficient photocatalytic activity [33–36]. However, the formation of new core-shell photocatalysts remains underexplored.

MoO<sub>3</sub> has been widely investigated as an electrode material for lithium-ion batteries. It has also attracted considerable interest as a promising material because of its low cost, non-toxicity, high adsorbability, and environmental biocompatibility [37–39]. Nevertheless, the commercial production of MoO<sub>3</sub> materials has been hindered due to the inherent electrical conductivity of this oxide, which results in low charge transfer ability. To improve its photocatalytic performance, MoO<sub>3</sub> is often combined with carbon materials or loaded with noble metals or metal oxides to further inhibit the rapid electron–hole recombination. Unfortunately, the photocatalytic activity of existing MoO<sub>3</sub> species is still far from adequate for practical application. The development of a suitable strategy for converting MoO<sub>3</sub> into practical photocatalysts remains a challenge. Thus, combining MoO<sub>3</sub> with MOFs is a novel approach. To date, only one kind of MoO<sub>3</sub>/MOF has been reported, i.e., MoO<sub>3</sub>/TMU-5, which displayed enhanced photo-oxidative desulfurization properties [40]. To the best of our knowledge, there is no report on MoO<sub>3</sub>/MOF-based photocatalysts for Cr(VI) photo-reduction.

Based on the aforementioned considerations, we developed a series of MoO<sub>3</sub>@ZIF-8 core-shell nanorod photocatalysts by a facile two-step method. The photocatalytic activity of the series of MoO<sub>3</sub>@ZIF-8 photocatalysts is characterized by Cr(VI) reduction under visible light. It is proved that a new bond is formed between MoO<sub>3</sub> and ZIF-8, which enhances the efficiency of separation of the photo-induced electron–hole pairs. The synergistic effect between MoO<sub>3</sub> and ZIF-8 has proven to boost the photocatalytic activity. Moreover, a possible mechanism for the photocatalytic process is proposed on the basis of the experimental results.

## 2. Experimental

### 2.1. Chemicals

Chemicals without special descriptions were obtained from commercial companies and used without further purification. Molybdenum powder, Zn(NO<sub>3</sub>)<sub>2</sub>·6H<sub>2</sub>O, 2-methylimidazole, methanol, hydrogen peroxide, Tert-Butanol (TBA), Benzoquinone (BQ), ethylene glycol, Polyvinylpyrrolidone (PVP) (M.W. 130,000) and 5,5-dimethyl-1-pyrrolone N-oxide (DMPO) were purchased from Sigma-Aldrich. Ultra-pure water with a resistance of 18.2 MΩ was prepared using a water purification system.

### 2.2. Sample preparation

#### 2.2.1. Preparation of MoO<sub>3</sub> nanowires

MoO<sub>3</sub> nanowires were synthesized via hydrothermal reaction. Typically, 2 g of Mo metal powder was added to 50 mL deionized water and stirred to form a homogenous mixture. Subsequently, H<sub>2</sub>O<sub>2</sub> solution (30 wt%; 80 mL) was added dropwise until the solution became light yellow and was stirred for 4 h after the color change. The solution was then transferred to a Teflon-lined stainless-steel autoclave, and the hydrothermal reaction proceeded at 180 °C for 120 h. The precipitate was washed several times with deionized water and ethanol for further use.

#### 2.2.2. Preparation of ZIF-8

Typically, 3.672 g Zn(NO<sub>3</sub>)<sub>2</sub>·6H<sub>2</sub>O was dissolved in 250 mL methanol (solution A). Afterwards, the solution B was prepared by dissolving 4.053 g 2-methylimidazole in another 250 mL methanol. After dissolution, two solutions were mixed directly. Subsequently, the mixed solution was stirred for 30 min at 40 °C. and allowed to keep still at ambient temperature for 24 h. Finally, the white precipitate was collected by centrifugation, washed with methanol, and dried at 80 °C

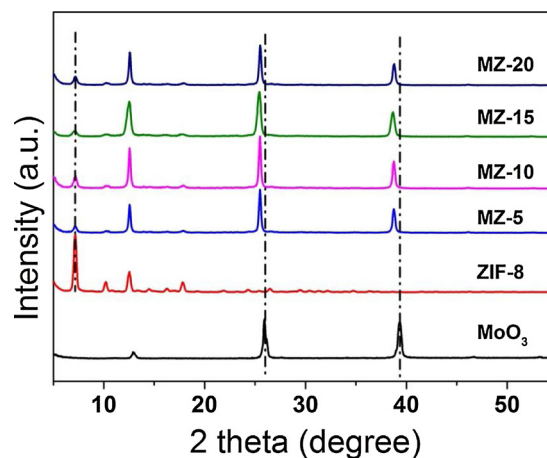


Fig. 1. (a) XRD patterns of as prepared samples.

overnight.

#### 2.2.3. Preparation of MoO<sub>3</sub>@ZIF-8 core-shell nanorods

First, 0.5 g of the as-prepared MoO<sub>3</sub> nanowires and 200 mg of PVP were dissolved in 50 mL of methanol under sonication (Solution C). Subsequently, 0.07 g Zn(NO<sub>3</sub>)<sub>2</sub>·6H<sub>2</sub>O was dissolved in 20 mL of methanol (Solution D) and 0.077 g of 2-methylimidazole was dissolved in 20 mL of methanol (Solution E). Solution D and Solution E were simultaneously added to Solution C. The mixed solution was stirred at 40 °C for 24 h. The as-prepared samples were washed with water and methanol several times and stored for further use. The as-prepared sample was denoted as MZ-10, based on the 10 wt% of ZIF-8. The other MoO<sub>3</sub>@ZIF-8 materials were denoted as MZ-5, MZ-10, MZ-15, and MZ-20 based on the various weight percentages of ZIF-8. The mechanism of formation of MoO<sub>3</sub>@ZIF-8 is schematically represented in Scheme 1.

### 2.3. Characterization

The structures of the samples were examined using X-ray diffraction (XRD, D2 PHASER, Bruker). The morphology was evaluated via scanning electron microscopy (SEM; Model SU8010, Hitachi Co., Ltd) and field-emission transmission electron microscope (FE-TEM) images were acquired using a JEM-2100 F instrument. The samples were also analyzed by X-ray photoelectron spectroscopy (XPS, VG Scientific Co., ESCA LAB MK-II). The specific surface areas of the samples were calculated using an adsorption analyzer (BEL BELSORP) based on adsorption data in the partial pressure (P/P<sub>0</sub>) range of 0.02–0.25. The UV–vis diffuse reflectance spectra (DRS, Hitachi U-3010 spectrophotometer) were obtained by the Kubelka-Munk approach with BaSO<sub>4</sub> as a reference at room temperature. Steady-state/time-resolved photoluminescence emission spectra (320 nm excitation) were measured at room temperature with a fluorescence spectrophotometer. Electron spin resonance (ESR) signals were recorded on a Bruker ESR A300 spectrometer at room temperature (298 K). Electrochemical impedance spectroscopy (EIS) were performed using an Ivium electrochemical analyzer with a conventional three-electrode system in which modified Ni foam, Ag/AgCl electrode, and Pt wire were employed as the working, reference, and counter electrodes, respectively. The conditions were as follows: 3 M NaSO<sub>4</sub> electrolyte, a frequency range from 0.1 Hz to 10 kHz, and an applied sine-wave potential of 5 mV amplitude.

### 2.4. Photocatalytic evaluation

The photocatalytic performance of the as-prepared samples was evaluated by using a solar simulator (Sun 2000, ABET) as a light source with a 440 nm cutoff filter. During each photocatalytic experiment,

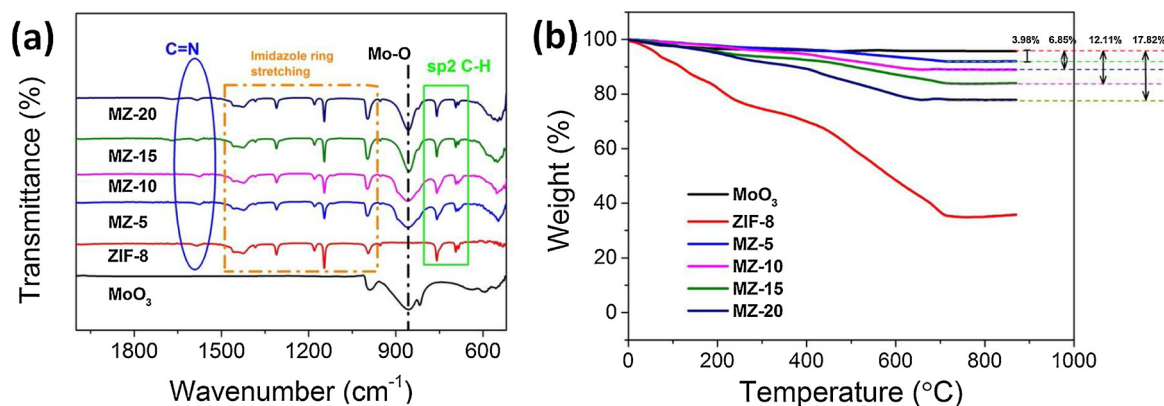


Fig. 2. (a) FT-IR patterns of the as prepared samples; (b) TGA analyses of the as prepared samples.

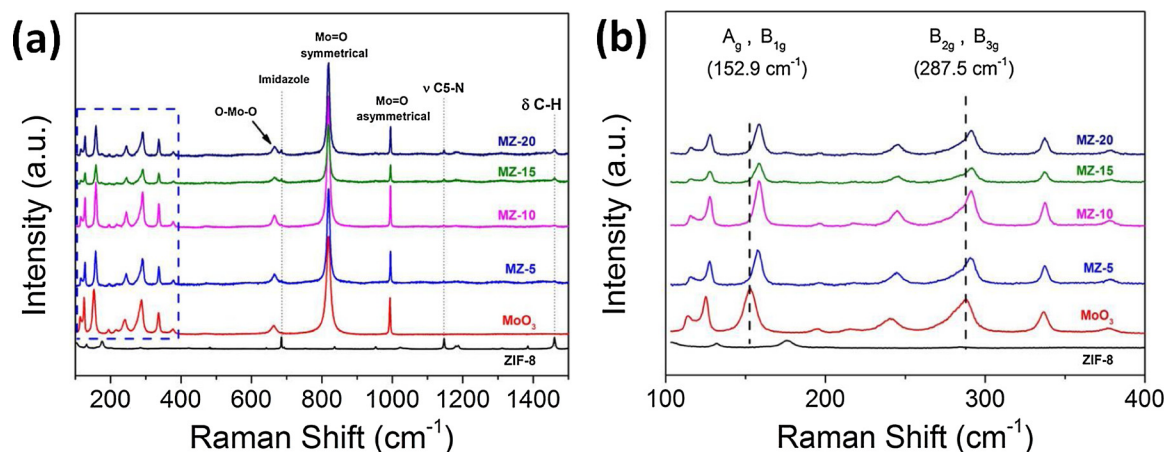


Fig. 3. (a) Raman spectra of the as prepared samples (100–1500 cm⁻¹); (b) Raman spectra of the as prepared samples (100–400 cm⁻¹) (central position of the A<sub>g</sub> and B<sub>g</sub> mode in MZ serial samples are shifted toward the longer wavenumbers).

50 mg of the as-prepared catalyst was dispersed in 100 ml of Cr(VI) aqueous solution (20 mg L<sup>-1</sup>). The suspension was sonicated for 120 min before the illumination process to reach adsorption-desorption equilibrium. During irradiation, ~4 mL of suspension was sampled and filtered with a syringe filter (0.22 μm) at 30 min intervals to remove the suspended photocatalysts. The concentration of Cr(VI) was determined from the peak intensity at 540 nm. In order to test the stability of the as-prepared catalysts, the used catalyst was collected by centrifugation and washed with water for the cycling test. The pure MoO<sub>3</sub> nanowires and ZIF-8 were prepared and tested under the same conditions.

### 3. Results and discussion

#### 3.1. Structure and composition

X-ray diffraction (XRD) served to detect the phases of the as prepared catalysts. As shown in Fig. 1, the MoO<sub>3</sub> nanowires with various ZIF-8 weight percentages showed clear crystal peaks. The diffraction peaks at 12.6, 25.4, and 38.8° could be indexed to the (0 2 0), (0 4 0), and (0 6 0) planes of MoO<sub>3</sub> (PDF No. 05-0508) [17], respectively. Meanwhile, the peaks of ZIF-8 are consistent with the previous reports. Interestingly, comparing with the other samples, the peaks of (0 2 0), (0 4 0), and (0 6 0) in other samples display an obvious shift to lower angles (Fig. 1), which can be attributed to the enlarged interlayer spacing. In order to have a deep sight into the layer structure of the as prepared samples, the Bragg equation  $2d\sin\theta = n\lambda$  ( $n = 1$ ,  $k = 0.154$  nm), where  $d$  is the distance of the parallel atomic plane,  $\lambda$  is the incident wavelength,  $\theta$  is the angle between incident light and crystal surface, was used to calculate the  $d$ -spacing values [41]. As we

know, the  $n$  and  $k$  are constant, so when the XRD peak shift to the lower angle ( $\theta$ ), the  $d$  is enlarged. The  $d$ -spacing values (0 2 0) of serial materials were calculated to be 0.350 nm (MoO<sub>3</sub>), 0.355 nm (MZ-5), 0.359 nm (MZ-10), 0.361 nm (MZ-15) and 0.365 nm (MZ-20), respectively. This result suggests that after depositing the ZIF-8 NPs, the distance of the parallel atomic plane were larger than pristine MoO<sub>3</sub> nanowires. Meanwhile, there were also some small peaks at 7.17°, which can be found in the XRD of ZIF-8 and MZ serial catalysts. Evidently, it proved from the side that ZIF-8 NPs were successfully deposited on the MoO<sub>3</sub> nanowires.

Structures of as-obtained materials were analyzed by FT-IR spectroscopy. As shown in Fig. 2(a), the FTIR of MZ-5, MZ-10, MZ-15 and MZ-20 exhibited the similar peaks at 652–806 cm<sup>-1</sup>, 963–1486 cm<sup>-1</sup> and 1582 cm<sup>-1</sup>, which can be respectively attributed to the sp<sup>2</sup> C-H, imidazole ring stretching and C=N bond of ZIF-8. Moreover, the FTIR of MZ-5, MZ-10, MZ-15 and MZ-20 also displayed a peak at 856 cm<sup>-1</sup>, which was assigned to the asymmetrical stretching vibration of the Mo-O bond of MoO<sub>3</sub>. Moreover, in order to investigate the actual weight percentage of ZIF-8 deposition and the thermal stability of the composite of ZIF-8 and MoO<sub>3</sub> nanowires, thermogravimetric analysis (TGA) curves of the as prepared samples was performed in the N<sub>2</sub> from 20 °C to 900 °C were conducted. As shown in Fig. 2(b), a total weight loss of about 65% was recorded for pure ZIF-8, corresponding to the decomposition of ZIF-8. Besides, the pure MoO<sub>3</sub> nanowires displayed a weight loss of 4%, presented a well thermal stability. The TG curves of the ZIF-8 modified MoO<sub>3</sub> nanowires followed a similar trend to that of ZIF-8. However, the weight loss of MZ-5, MZ-10, MZ-15 and MZ-20 was around 3.98, 6.85, 12.11 and 17.82%, respectively. Thus, the actual loading of the deposited ZIF-8 on the MoO<sub>3</sub> was calculated to be 3.98,



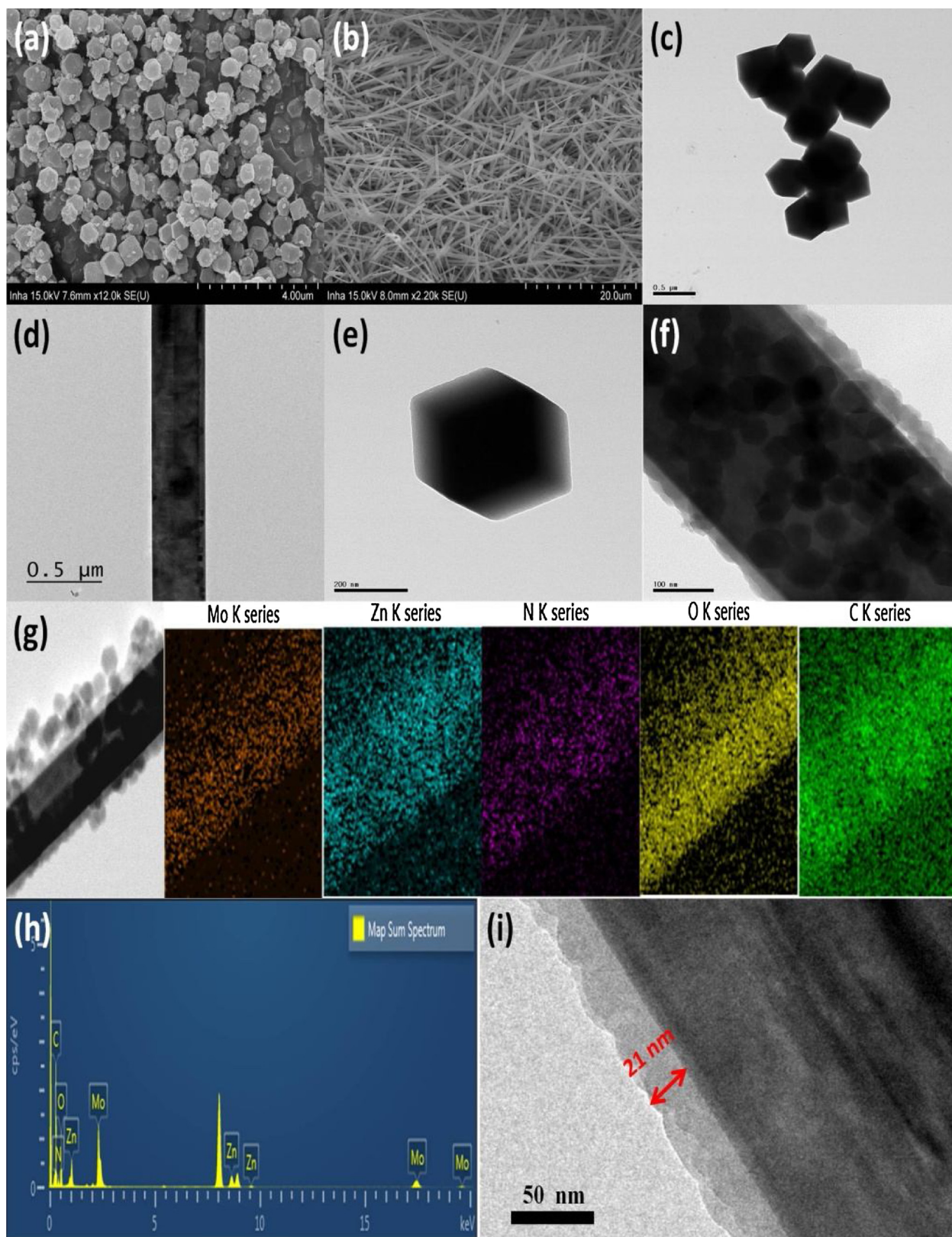


**Fig. 4.** (a) SEM of ZIF-8; (b) SEM of MoO<sub>3</sub> nanowires; (c) TEM of ZIF-8; (d) and (e) TEM images of MoO<sub>3</sub> nanowires and ZIF-8 nanoparticles; (f) TEM of MoO<sub>3</sub>@ZIF-8 core-shell nanorods (MZ-15); (g) elemental mapping patterns of MoO<sub>3</sub>@ZIF-8 core-shell nanorods; (h) EDX spectrum of MoO<sub>3</sub>@ZIF-8 core-shell nanorods; (i) HRTEM images of MoO<sub>3</sub>@ZIF-8 core-shell nanorods.

6.85, 12.11 and 17.82%, respectively. It is understandable that the actual contents of deposited ZIF-8 on MoO<sub>3</sub> nanowires were somewhat less than the designed value.

Raman spectroscopy was applied to reveal the vibrational modes of the various samples. As shown in Fig. 3(a), all of the MZ serial samples presented three Raman peaks, corresponding to the O-Mo-O,

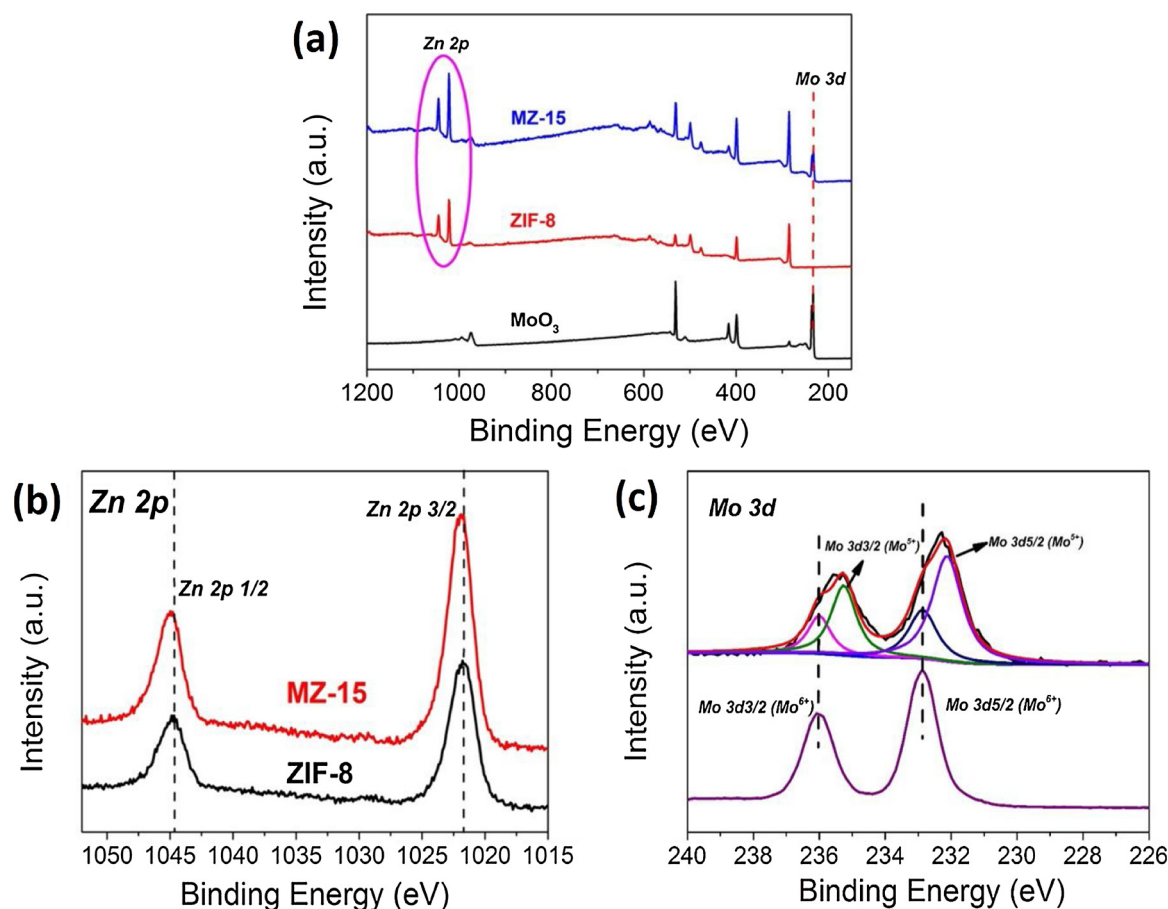


Fig. 5. XPS of as prepared samples: (a) survey spectra of as prepared samples ( $\text{MoO}_3$ , ZIF-8 and MZ-15); (b) Zn 3d of  $\text{MoO}_3$  and MZ-15; (c) Mo 3d of  $\text{MoO}_3$  and MZ-15.

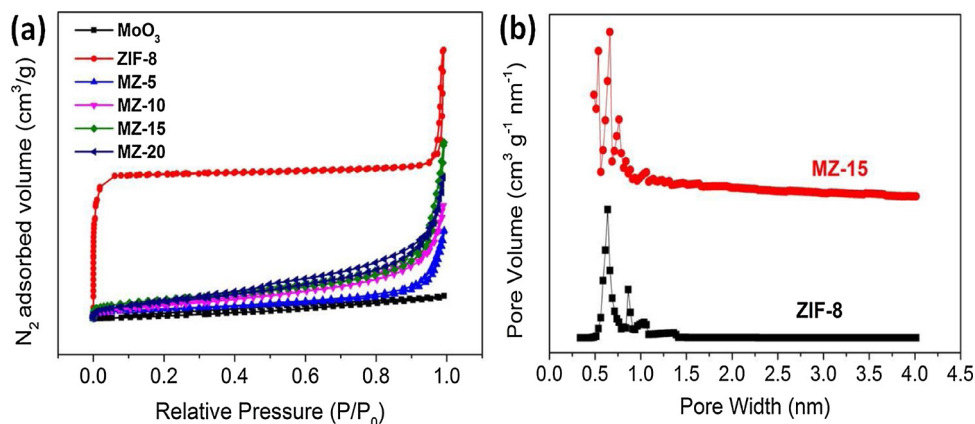


Fig. 6. (a)  $\text{N}_2$  adsorption-desorption isotherm of the as prepared samples; (b) pore size distribution of ZIF-8 and MZ-15.

symmetrical  $\text{Mo}=\text{O}$ , and asymmetrical  $\text{Mo}=\text{O}$  vibrations derived from the  $\text{MoO}_3$  nanowires. Meanwhile, the Raman peaks of ZIF-8 was recorded and the results were consistent with the previous reports. The peaks at  $686.1$ ,  $1142.3$ , and  $1461.4 \text{ cm}^{-1}$  can be assigned to the imidazole,  $\nu \text{ C5-N}$ , and  $\delta \text{ C-H}$ , respectively [42]. Intercomparison of the samples showed that all of the MZ series samples possessed these Raman peaks of ZIF-8. Therefore, it can be deduced that ZIF-8 was successfully loaded onto the  $\text{MoO}_3$  nanowires. The  $158 \text{ cm}^{-1}$  ( $A_g$ ,  $B_{1g}$ ) band in Fig. 3(b) originates from translation of the rigid chains, and the  $285 \text{ cm}^{-1}$  ( $B_{2g}$ ,  $B_{3g}$ ) band is a doublet derived from the wagging modes of the terminal oxygen atoms of  $\text{MoO}_3$  [43]. Interestingly, compared with the  $\text{MoO}_3$  nanowires, the peaks of the  $A_g$  and  $B_g$  mode showed a clear red shift toward to higher wavenumbers. This Raman shift is

associated with a decrease in the bond stretching frequency of the as-prepared samples, suggesting that  $\text{MoO}_3$  and ZIF-8 were combined with each other, which is consistent with the XRD and TEM data.

The morphology and microstructure of the as prepared samples were analyzed by SEM, TEM and HRTEM. Fig. 4(a) and (b) show the presence of wire-like  $\text{MoO}_3$  with a diameter of 200–400 nm and the cube structure of ZIF-8. Fig. 4(c)–(e) illustrate TEM images of  $\text{MoO}_3$  nanowires and ZIF-8 NPs. Besides, the  $\text{MoO}_3$ @ZIF-8 core-shell nanorods (MZ-15) were also displayed by HRTEM to further confirm a core-shell structure (Fig. 4(f)). TEM images of MZ-5, MZ-10, MZ-15, and MZ-20 were also shown in the Fig. S1. As we know, this core-shell structure is beneficial for charge/mass transport and light adsorption. The corresponding elemental mappings in Fig. 4(g) shows that the  $\text{MoO}_3$ @ZIF-8

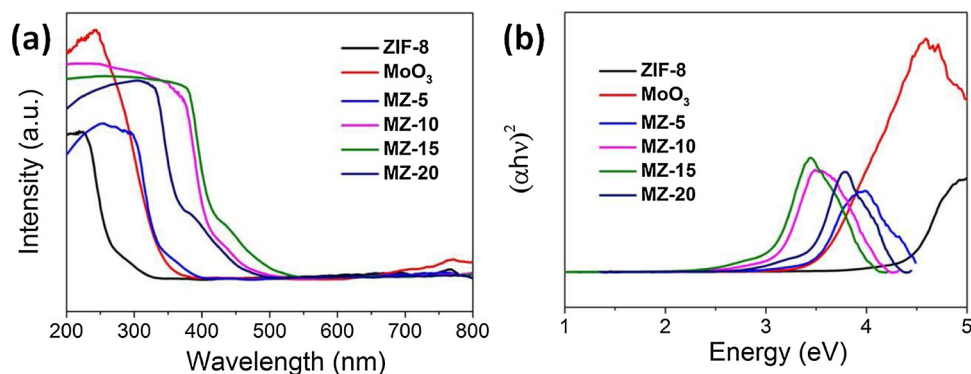


Fig. 7. (a) UV-vis DRS spectra of the as-prepared samples; (b) corresponding plots of  $(\alpha h\nu)^2$  versus photon energy ( $h\nu$ ).

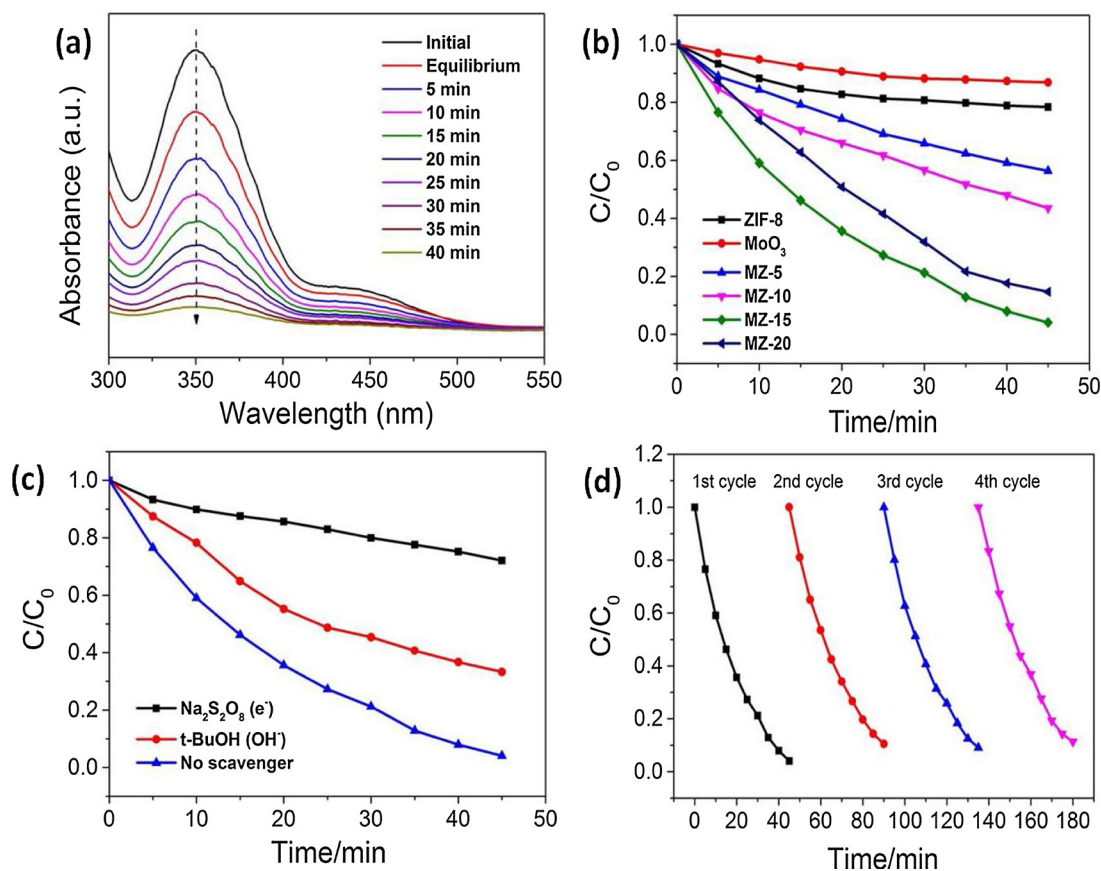


Fig. 8. (a) Time-dependent degradation spectral pattern of Cr(VI) solutions over MZ-15; (b) Photocatalytic performance of MZ-15 under visible light irradiation (c) Photocatalytic performance of MZ-15 with different species of quenchers ( $\text{Na}_2\text{S}_2\text{O}_8$  for  $\text{e}^-$ ,  $\text{t-BuOH}$  for  $\text{OH}^\cdot$ ); (d) cycling runs of MZ-15.

core-shell nanorods consists of Mo, O, Zn, C and N, indicating that  $\text{MoO}_3$ @ZIF-8 core-shell nanorods were successfully synthesized, which is consistent with the EDX spectra (Fig. 4(h)). Fig. 4(i) show a pronounced core-shell structure of  $\text{MoO}_3$ @ZIF-8 composites with a shell thickness of approximately 21 nm. Meanwhile, the TEM images of MZ-15 before and after the cycling were also displayed to confirm the stability of catalyst (Fig. S4).

The chemical states of the as prepared samples were examined by X-ray photoelectron spectroscopy (XPS). Fig. 5(a) shows the survey spectra of as prepared samples ( $\text{MoO}_3$ , ZIF-8 and MZ-15). It is clear that Zn 2p peaks are all observed in both ZIF-8 and MZ-15. Meanwhile, the Mo 3d peaks are only observed in  $\text{MoO}_3$  and MZ-15 which is the evidence that  $\text{MoO}_3$ @ZIF-8 core-shell nanorods were synthesized successfully. Besides, Fig. 5(b) shows the Zn 2p spectrum of  $\text{MoO}_3$  and MZ-15, which indicates that the ZIF-8 NPs are decorated on the surface of

$\text{MoO}_3$ . From Fig. 5(b), the binding energy peaks of Zn 2p  $1/2$  and Zn 2p  $3/2$  of ZIF-8 NPs are located at 1044.8 and 1021.8 eV, respectively. Compared with the MZ-15, the Zn 2p peaks in the MZ-15 are located at 1045.1 and 1022.1 eV, which shift slightly about 0.3 eV toward higher binding energies owing to the interaction between ZIF-8 and  $\text{MoO}_3$ , in which Zn can act as an electron donor. Similar observations have been by previous reports [44]. As displayed in Fig. 5(c), two peaks of the  $\text{Mo}^{6+}$  species ( $\text{MoO}_3$  nanowires) were observed at 236.1 and 232.9 eV, which were ascribed to the Mo 3d $3/2$  and Mo 3d $5/2$  states, respectively. Compared to  $\text{MoO}_3$ , the chemical state of MZ-15 differed significantly. As shown in Fig. 5(c), new peaks were observed at 235.3 and 232.1 eV, which can be ascribed to Mo 3d $3/2$  ( $\text{Mo}^{5+}$ ) and Mo 3d $5/2$  ( $\text{Mo}^{5+}$ ). Thus, we can deduce that  $\text{Mo}^{6+}$  species are partially reduced after combination with the ZIF-8. Thus, we can deduce that the ZIF-8 and  $\text{MoO}_3$  had been combined with each other [45,46].



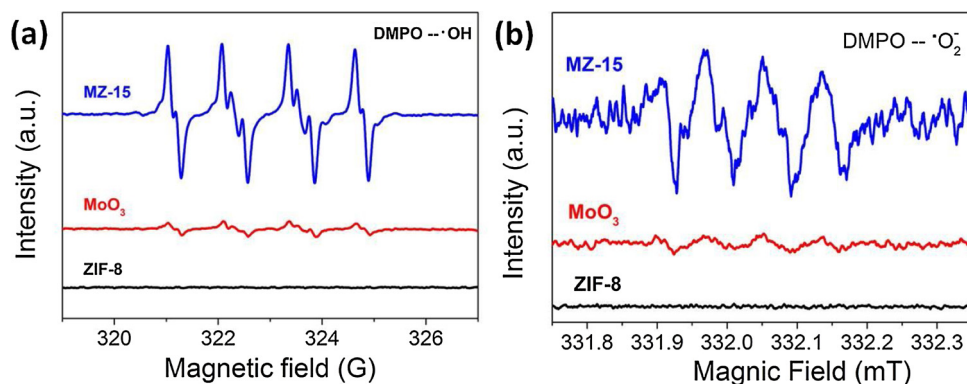


Fig. 9. (a) DMPO spin-trapping ESR spectra of as prepared samples for  $\cdot\text{OH}$  (under simulated visible light irradiation); (b) DMPO spin-trapping ESR spectra of as prepared samples for  $\cdot\text{O}_2^-$  (under simulated visible light irradiation).

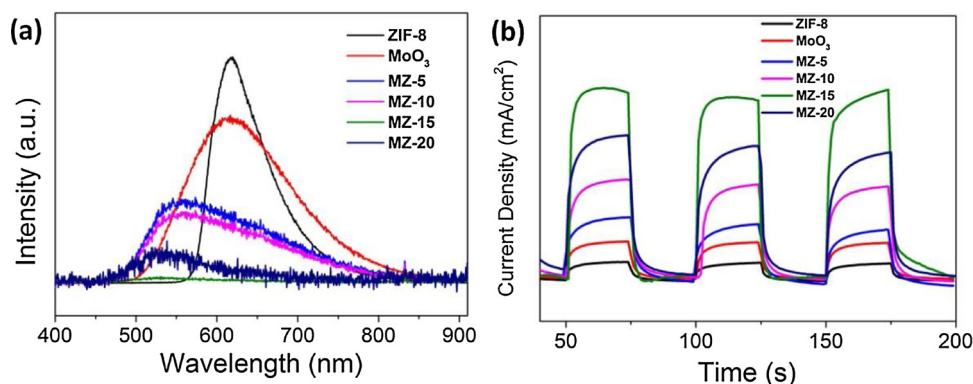


Fig. 10. (a) PL spectra of the as-prepared samples; (b) Transient photocurrent response of the as-prepared samples.

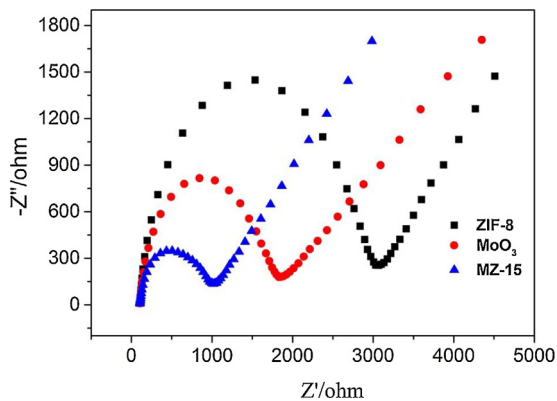


Fig. 11. (a) EIS spectroscopy of as-prepared samples.

As shown in Fig. 6(a) and (b), the nitrogen physisorption measurements indicate that microporous nature of the ZIF-8 NPs. Meanwhile, the specific surface area of ZIF-8 is as high as  $1531.1 \text{ m}^2/\text{g}$ , which is a good adsorbent and will provide more active sites during the reaction. Besides, in virtue of the high surface area of the ZIF-8, when it is combined with  $\text{MoO}_3$ , the specific surface area is improved. The specific surface area of the  $\text{MoO}_3$ , MZ-5, MZ-10, MZ-15, and MZ-20 are 49.8, 98.4, 120.6, 212.7 and  $287.6 \text{ m}^2/\text{g}$ , respectively (Fig. 6(a)). The core-shell nanostructure will not only impede their aggregation by drastically decreasing interaction locations but also effectively enhances the number of the active sites. According to the classification of pores (IUPAC), the pore size under the 2 nm was called micropore, pore size less than 0.7 nm are called ultramicropore. As shown in Fig. 6(b), we use the HorvathKawazoe (HK) method to reveal the pore size distribution of our samples and plentiful micropores in both ZIF-8 and

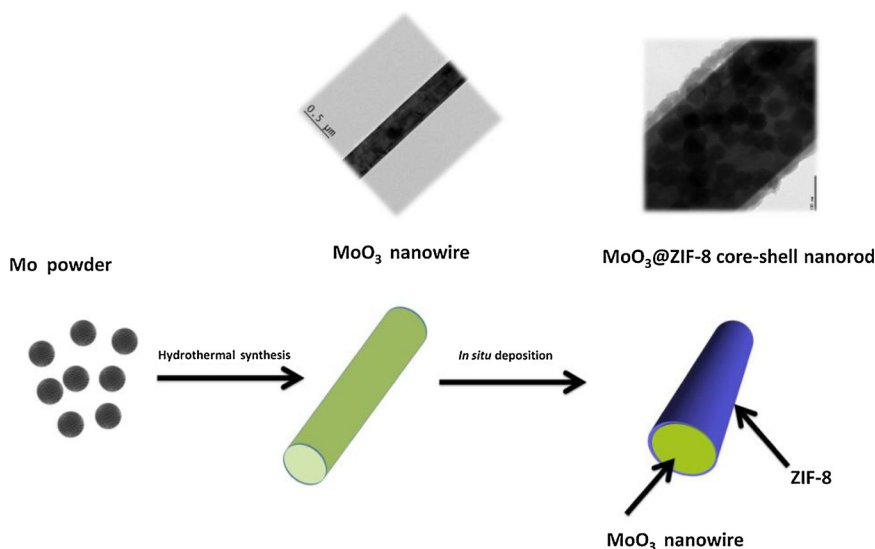
MZ-15 were observed. The specific surface area of the MZ-15 nanotubes is 4.2 times higher than that of the  $\text{MoO}_3$  nanowires. The core shell structures result in a high surface area, which significantly enhance the photocatalytic ability by accelerating charge separation and transfer [14].

To further reveal the intrinsic mechanism of the as-prepared samples, DRS spectrums were obtained. The optical absorption properties of as prepared samples were displayed in Fig. 7(a). After the depositing of ZIF-8 NPs on the  $\text{MoO}_3$  nanowires, the light adsorption range of MZ composites photocatalysts showed a red shift when comparing with pure  $\text{MoO}_3$  and ZIF-8. It may be the effect of the interface between  $\text{MoO}_3$  and ZIF-8. On the other hand, an obvious red shift in DRS indicates a higher light adsorption ability. As reported previously, the band gaps ( $E_g$ ) of the semiconductor was calculated by the following equation [47]

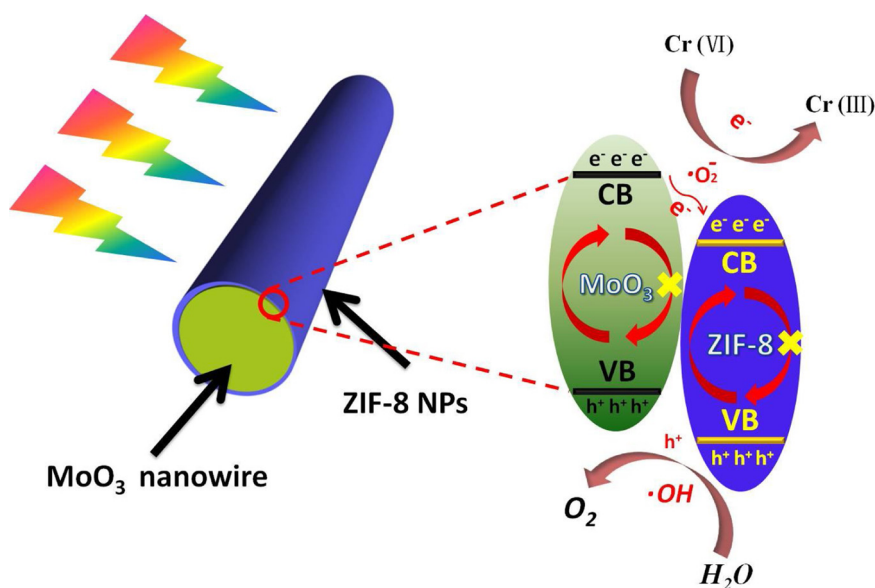
$$\alpha h\nu = A(h\nu - E_g)^{n/2} \quad (1)$$

where  $\alpha$ ,  $\nu$ ,  $E_g$ , and  $A$  are the absorbance coefficient, light frequency, band gap energy, and a constant, respectively. The value of  $n$  is determined by the type of optical transition ( $n = 1$  for direct transition and  $n = 4$  for indirect transition). Therefore, the  $E_g$  of as-prepared samples were determined from the plot of  $(\alpha h\nu)^2$  versus  $h\nu$ , as shown in Fig. 7(b). The band gaps for ZIF-8,  $\text{MoO}_3$ , MZ-5, MZ-10, MZ-15, and MZ-20 were found to be 4.44, 3.54, 3.44, 3.25, 2.95, and 3.12 eV, respectively.

A pronounced enhancement in the light absorption was achieved as the ZIF-8 content was progressively increased, indicating that modification with ZIF-8 can improve the light absorption ability of  $\text{MoO}_3$  owing to the formation of a nanojunction between ZIF-8 and  $\text{MoO}_3$ . These results suggest that ZIF-8 was successfully loaded on the  $\text{MoO}_3$  nanowires, and the light absorption capacity was enhanced, thus improving the catalytic activity.



**Scheme 1.** Schematic illustration of the synthetic procedure for the hollow  $\text{MoO}_3$ @ZIF-8 core-shell nanorods.



**Scheme 2.** Schematic illustration of the Cr(VI) degradation mechanism.

The typical temporal evolution of the spectra of the Cr(VI) solutions over MZ-15 is presented in Fig. 8(a); the samples were withdrawn from the reactor at 5 min intervals. The absorption peak at 350 nm, which is ascribed to Cr(VI), decreased rapidly with the irradiation time, and almost disappeared after 40 min of illumination. In addition, the photocatalytic degradation of Cr(VI) over all of the as-prepared samples is shown in Fig. 8(b). The Cr(VI) absorption rapidly decreased over MZ-15, reaching 96% degradation within 40 min. For comparison, the catalytic performance of the  $\text{MoO}_3$  nanowires (20%) and ZIF-8 nanosheets (13%) over the course of 40 min was much lower than that of MZ-15. The performance of MZ-5, MZ-10, and MZ-20 was also examined under the same conditions. The rate of Cr(VI) degradation with the as-prepared catalysts followed the order: MZ-15 > MZ-20 > MZ-10 > MZ-5 > ZIF-8 >  $\text{MoO}_3$ . The efficiency of MZ-15 was 7.4 and 4.6 times higher than that of bare  $\text{MoO}_3$  and ZIF-8, respectively. For the series of MZ catalysts, MZ-15 displayed the best performance. This indicates that the optimum ZIF-8 loading was 12.11% (Fig. 2(b)). Furthermore, the quantum efficiency (QE) of  $\text{MoO}_3$ , ZIF-8, and MZ-15 was determined, and the results are shown in Table S1. The highest QE constant was obtained for MZ-15, indicating an improvement in the

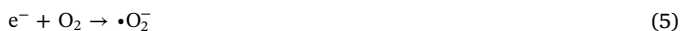
photocatalytic activity with ZIF-8 loading [16]. To further examine the mechanism of Cr(VI) degradation, active species ( $\cdot\text{OH}$  and  $e^-$ ) trapping experiments were performed (Fig. 8(c)). For MZ-15, the Cr(VI) degradation rate was suppressed by adding  $\cdot\text{OH}$  (*t*-BuOH, 1 mM) and  $e^-$  radical scavengers ( $\text{Na}_2\text{S}_2\text{O}_8$ , 1 mM). This indicates that both  $\cdot\text{OH}$  and  $e^-$  are crucial for the photocatalytic reaction. To confirm the photocatalytic stability, MZ-15 was used in repetitive Cr(VI) photodegradation cycles under the same conditions. As shown in Fig. 8(d), after four cycles, the photocatalytic activity of MZ-15 remained almost unchanged. The XRD patterns (Fig. S2) reveal that MZ-15 remained unchanged after four rounds of the catalytic reaction, which clearly indicates its stability. Further, the absence of significant changes in the XPS (Fig. S3) profile (before and after cycling) reveal that the components and crystal structure were stable during the reaction.

To further probe the effect of the  $\cdot\text{OH}$  and  $\cdot\text{O}^-$  radical scavengers, the DMPO spin-trapping ESR technique was used. Fig. 9(a) shows the ESR spectra ( $\cdot\text{OH}$ ) acquired under photo-irradiation of the as-prepared samples. Almost no ESR signal was observed for the ZIF-8 and  $\text{MoO}_3$  nanowires. However, an obvious ESR signal was observed for MZ-15, proving that the  $\text{OH}^-$  can be transformed to  $\cdot\text{OH}$  by oxidization, and



the  $\cdot\text{OH}$  can be further oxidized by the photo-generated holes to form  $\text{O}_2$ . The ESR signal of  $\cdot\text{O}^-$  observed for MZ-15 was much higher than that of ZIF-8 and  $\text{MoO}_3$  (Fig. 9(b)). A number of previous studies proved that  $\text{Cr(VI)}$  can be further reduced to  $\text{Cr(III)}$  by photo-generated electrons [7]. Therefore, the electrons produced by MZ-15 can reduce  $\text{Cr(VI)}$  to  $\text{Cr(III)}$ .

Based on these results,  $\text{Cr(VI)}$  reduction over MZ-15 can be described by the following reactions:



To confirm the generation, transfer, and separation of the photo-induced electrons and holes, the photoluminescence (PL) spectra and transient photocurrent density of the as-prepared samples were analyzed (Fig. 10(a) and (b)). As shown in Fig. 10(a), the lower PL intensity indicates better separation and transfer of the charge carriers. The PL intensity of MZ-15 was the lowest among that of the samples tested, which indicates that electron–hole separation occurred fastest for MZ-15. Photocurrent experiments were performed with intermittent visible-light irradiation for intervals of 25 s. A higher photocurrent response indicates better separation of the photo-induced electrons and holes. As shown in Fig. 10(b), the photocurrent density of MZ-15 was highest among that of the samples, in agreement with the photocatalytic activity sequence.

EIS analysis was performed to examine charge separation and transfer at the solid-solution interface. The Nyquist plot for MZ-15 in shown in Fig. 11, as a representative plot; this sample produced the smallest arc radius among the as-prepared samples. The observed smaller arc radius indicates that the charge transfer resistance of MZ-15 decreased remarkably owing to the formation of the ZIF-8 NPs on the surface. As we know, flexible supporting materials will provide more space for the proton transportation. Xu et al. [48,49] first prepared a MOF-incorporated proton exchange membranes and studied its proton conductivity. Zhu et al. [50] fabricated MOF–polymer composite membranes, the results displayed an improvement in the conductivity. Meanwhile, the high surface area of ZIF-8 NPs will provide more active sites for the electrons and protons. So the conductivity of MZ is enhanced. Generally, a low resistance is beneficial for charge transfer, and should enhance utilization of the photogenerated holes and electrons and improve the photocatalytic activity.

Based on the experimental results presented above, a possible mechanism for the enhanced photocatalytic activity of MZ-15 was proposed (Scheme 2). The PL spectra and photocurrent analysis show that the prepared MZ-15 formed a heterojunction, which can improve the charge separation efficiency (Fig. 10). Hence, more electrons from the conduction band (CB) of  $\text{MoO}_3$  can be transferred to ZIF-8. As a result, MZ-15 can reduce  $\text{Cr(VI)}$  to  $\text{Cr(III)}$ . In other words,  $\text{MoO}_3$  can be excited by light irradiation, and electron–hole pairs are simultaneously generated. However, the electrons and holes easily recombine in the absence of the ZIF-8 NPs. After the introduction of ZIF-8, the “synergistic effect” between  $\text{MoO}_3$  and ZIF-8 will enhance the electron trapping ability and photocatalytic activity of the composite.

#### 4. Conclusions

In summary, a heterogeneous  $\text{MoO}_3$ @ZIF-8 core-shell nanorods heterojunction photocatalyst was successfully synthesized using a facile method. The formation of ZIF-8 NPs on the surface of  $\text{MoO}_3$  nanowires was confirmed by various characterization methods. Interestingly,  $\text{MoO}_3$ @ZIF-8 core-shell nanorods, as a novel photocatalyst,

demonstrated excellent stability and activity for  $\text{Cr(VI)}$  degradation. The enhanced photocatalytic activity is mainly derived from the synergistic effect and lower electron–hole recombination rate, which promotes the utilization of light and photogeneration of charge carriers, resulting in an enhancement of the  $\text{Cr(VI)}$  degradation.

#### Acknowledgment

This work was supported by an Inha University Research Grant, South Korea.

#### Appendix A. Supplementary data

Supplementary material related to this article can be found, in the online version, at doi:<https://doi.org/10.1016/j.apcatb.2018.08.077>.

#### References

- [1] D. Blowes, Tracking hexavalent Cr in groundwater, *Science* 295 (2002) 2024–2025.
- [2] S. Rengaraj, S. Venkataraj, J.-W. Yeon, Y. Kim, X. Li, G. Pang, *Appl. Catal. B: Environ.* 77 (2007) 157–165.
- [3] Y. Li, Y. Bian, H. Qin, Y. Zhang, Z. Bian, *Appl. Catal. B–Environ.* 206 (2017) 293–299.
- [4] A.D. Bokare, W. Choi, *J. Environ. Sci. Technol.* 44 (2010) 7232–7237.
- [5] H. Chen, Y. Shao, Z. Xu, H. Wan, Y. Wan, S. Zheng, D. Zhu, *Appl. Catal. B–Environ.* 255 (2011) 255–262.
- [6] Y.Z. Yan, Q.D. An, Z.Y. Xiao, S.R. Zhai, B. Zhai, Z. Shi, *J. Mater. Chem. A* 5 (2017) 17073–17087.
- [7] C.C. Wang, X.D. Du, J. Li, X.X. Guo, P. Wang, J. Zhang, *Appl. Catal. B: Environ.* 193 (2016) 198–216.
- [8] Y.C. Zhang, L. Yao, G. Zhang, D.D. Dionysiou, J. Li, X. Du, *Appl. Catal. B: Environ.* 144 (2014) 730–738.
- [9] Y. Xing, A. Xueming Chen, D. Wang, *Environ. Sci. Technol.* 41 (2007) 1439–1443.
- [10] U. Divrikli, A.A. Kartal, M. Soyak, L. Elci, J. Hazard. Mater. 145 (2007) 459–464.
- [11] B. Xie, C. Shan, Z. Xu, X. Li, X. Zhang, J. Chen, B. Pan, *Chem. Eng. J.* 308 (2016) 791–797.
- [12] N. Li, Y. Tian, J. Zhao, J. Zhang, J. Zhang, W. Zuo, Y. Ding, *Appl. Catal. B: Environ.* 214 (2017) 126–136.
- [13] Y.F. Zhang, S.J. Park, *Carbon* 122 (2017) 287.
- [14] P. Zhang, T. Song, T. Wang, H. Zeng, *Appl. Catal. B Environ.* 206 (2017) 328–335.
- [15] Y.F. Zhang, S.J. Park, *J. Catal.* 355 (2017) 1–10.
- [16] P. Zhang, T. Song, T. Wang, H. Zeng, *Appl. Catal. B Environ.* 225 (2018) 172–179.
- [17] Y.F. Zhang, S.J. Park, *J. Catal.* 361 (2018) 238–247.
- [18] P. Zhang, T. Song, T. Wang, H. Zeng, *J. Mater. Chem. A* 5 (2017) 22772–22781.
- [19] S. Zhao, Y. Wang, J. Dong, C.-T. He, H. Yin, P. An, K. Zhao, X. Zhang, C. Gao, L. Zhang, J. Lv, J. Wang, J. Zhang, A.M. Khattak, N.A. Khan, Z. Wei, J. Zhang, S. Liu, H. Zhao, Z. Tang, *Nat. Energy* 1 (2016) 1–10.
- [20] M. Wen, K. Mori, T. Kamegawa, H. Yamashita, *Chem. Commun.* 50 (2014) 11645–11648.
- [21] F. Cao, M. Zhao, Y. Yu, B. Chen, Y. Huang, J. Yang, X. Cao, Q. Lu, X. Zhang, Z. Zhang, C. Tan, H. Zhang, *J. Am. Chem. Soc.* 138 (2016) 6924–6927.
- [22] M. Wen, K. Mori, Y. Kuwahara, T. An, H. Yamashita, *Chem. Asian J.* 13 (2018) 1767–1779.
- [23] M. Wen, K. Mori, Y. Kuwahara, T. An, H. Yamashita, *Appl. Catal. B Environ.* 218 (2017) 555–569.
- [24] P. He, X.-Y. Yu, X.W. Lou, *Angew. Chem. Int. Ed.* 56 (2017) 3897–3900.
- [25] M.-S. Yao, W.-X. Tang, G.-E. Wang, B. Nath, G. Xu, *Adv. Mater.* 28 (2016) 5229–5234.
- [26] R. Liang, R. Chen, F. Jing, N. Qina, L. Wu, *Dalton Trans.* 44 (2015) 18227–18236.
- [27] M. Ji, X. Lan, Z. Han, C. Hao, J. Qiu, *Inorg. Chem.* 51 (2012) 12389–12394.
- [28] T. Araya, S. Quan, J. Man-ke, M. Wan-hong, D. Johnson, H. Ying-ping, *Water Air Soil Pollut.* 227 (2016) 284.
- [29] K.G.M. Laurier, F. Vermoortele, R. Ameloot, D.E. De Vos, J. Hofkens, M.B.J. Roeffaers, *J. Am. Chem. Soc.* 135 (2013) 14488–14491.
- [30] P. Küsgens, M. Rose, I. Senkovska, H. Fröde, A. Henschel, S. Siegle, S. Kaskel, *Microporous Mesoporous Mater.* 120 (2009) 325–330.
- [31] J. Li, W. Ma, Y. Huang, X. Tao, J. Zhao, Y. Xu, *Appl. Catal. B: Environ.* 48 (2004) 17–24.
- [32] R. Lin, L. Shen, Z. Ren, W. Wu, Y. Tan, H. Fu, J. Zhang, L. Wu, *Chem. Commun.* 50 (2014) 8533.
- [33] Y. Zhang, Q. Li, C. Liu, X. Shan, X. Chen, W. Dai, X. Fu, *Appl. Catal. B* 224 (2018) 283–294.
- [34] Y.J. Yu, C. Yu, Y.Z. Niu, J. Chen, Y.L. Zhao, Y.C. Zhang, R.F. Gao, J.L. He, *Biosens. Bioelectron.* 101 (2018) 297.
- [35] D.K. Wang, Z.H. Li, *J. Catal.* 342 (2016) 151.
- [36] Z.Y. Yan, F. Wang, P.Y. Deng, Y. Wang, K. Cai, Y.H. Chen, Z.H. Wang, Y. Liu, *Biosens. Bioelectron.* 109 (2018) 132–138.
- [37] K. Cui, L. Yang, Z. Ma, F. Yan, K. Wu, Y. Sang, H. Chen, Y. Li, *Appl. Catal. B Environ.* 219 (2017) 592–602.
- [38] B. Feng, Z. Wu, J. Liu, K. Zhu, Z. Li, X. Jin, Y. Hou, Q. Xi, M. Cong, P. Liu, Q. Gu,

- Appl. Catal. B Environ. 206 (2017) 242–251.
- [39] Y. Peng, W. Si, X. Li, J. Luo, J. Li, J. Crittendenb, J. Hao, Appl. Catal. B Environ. 181 (2016) 692–698.
- [40] M. Bagheri, M.Y. Masoomi, A. Morsali, ACS Catal. 7 (10) (2017) 6949–6956.
- [41] D. Shan, S. Deng, J. Li, H. Wang, C. He, G. Cagnetta, B. Wang, Y. Wang, J. Huang, G. Yu, Carbon 119 (2017) 101–109.
- [42] O. Kolmykov, J.M. Commenge, H. Alem, E. Giroto, K. Mozet, G. Medjahdi, R. Schneider, Mater. Des. 122 (2017) 31–41.
- [43] B.C. Windom, W.G. Sawyer, D.W. Hahn, Tribol. Lett. 42 (2011) 301–310.
- [44] L. Deng, J. Zhu, X. Chen, M. Ding, H. Liu, J. Alloys Compd. 739 (2018) 1015–1024.
- [45] J. Wang, L. Tang, G. Zeng, Y. Deng, H. Dong, Y. Liu, L. Wang, B. Peng, C. Zhang, F. Chen, Appl. Catal. B: Environ. 222 (2018) 115–123.
- [46] X. Tu, S. Luo, G. Chen, J. Li, Chem. A Eur. J. 18 (2012) 14359–14366.
- [47] Y. Zhang, M. Park, H.Y. Kim, B. Ding, S.-J. Park, Appl. Surf. Sci. 384 (2016) 192–199.
- [48] B. Wu, X. Lin, L. Ge, L. Wua, T. Xu, Chem. Commun. 49 (2013) 143–145.
- [49] B. Wu, L. Ge, X. Lin, L. Wu, J. Luo, T. Xu, J. Membr. Sci. 458 (2014) 86–95.
- [50] X. Liang, F. Zhang, W. Feng, X. Zou, C. Zhao, H. Na, C. Liu, F. Sun, G. Zhu, Chem. Sci. 4 (2013) 983–992.